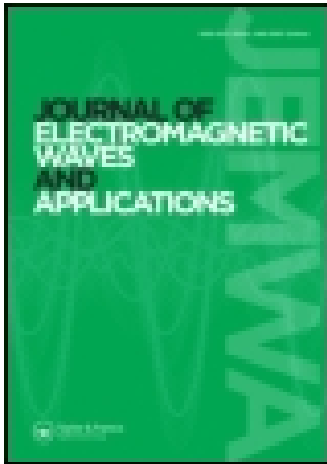


This article was downloaded by: [EPFL Bibliothèque]

On: 07 July 2015, At: 09:13

Publisher: Taylor & Francis

Informa Ltd Registered in England and Wales Registered Number: 1072954 Registered office: 5 Howick Place, London, SW1P 1WG



Journal of Electromagnetic Waves and Applications

Publication details, including instructions for authors and subscription information:

<http://www.tandfonline.com/loi/tewa20>

Theoretical and experimental analysis of subwavelength bowtie-shaped antennas

Arif E. Cetin^{abcd}, Serap Aksu^{ef}, Mustafa Turkmen^{ag}, Dordaneh Etezadi^{ab} & Hatice Altug^b

^a Department of Electrical and Computer Engineering, Boston University, Boston, MA 02215, USA

^b Bioengineering Department, EPFL, Lausanne CH-1015, Switzerland

^c Department of Biological Engineering, Massachusetts Institute of Technology, Cambridge, MA 02139, USA

^d Koch Institute for Integrative Cancer Research, Massachusetts Institute of Technology, Cambridge, MA 02139, USA

^e Division of Materials Science and Engineering, Boston University, Boston, MA 02215, USA

^f Department of Biosystems Science and Engineering, ETH Zürich, Basel 4058, Switzerland

^g Department of Electrical and Electronics Engineering, Erciyes University, Kayseri 38039, Turkey

Published online: 07 Jul 2015.



CrossMark

[Click for updates](#)

To cite this article: Arif E. Cetin, Serap Aksu, Mustafa Turkmen, Dordaneh Etezadi & Hatice Altug (2015): Theoretical and experimental analysis of subwavelength bowtie-shaped antennas, Journal of Electromagnetic Waves and Applications, DOI: [10.1080/09205071.2015.1051188](https://doi.org/10.1080/09205071.2015.1051188)

To link to this article: <http://dx.doi.org/10.1080/09205071.2015.1051188>

PLEASE SCROLL DOWN FOR ARTICLE

Taylor & Francis makes every effort to ensure the accuracy of all the information (the "Content") contained in the publications on our platform. However, Taylor & Francis, our agents, and our licensors make no representations or warranties whatsoever as to the accuracy, completeness, or suitability for any purpose of the Content. Any opinions and views expressed in this publication are the opinions and views of the authors,

and are not the views of or endorsed by Taylor & Francis. The accuracy of the Content should not be relied upon and should be independently verified with primary sources of information. Taylor and Francis shall not be liable for any losses, actions, claims, proceedings, demands, costs, expenses, damages, and other liabilities whatsoever or howsoever caused arising directly or indirectly in connection with, in relation to or arising out of the use of the Content.

This article may be used for research, teaching, and private study purposes. Any substantial or systematic reproduction, redistribution, reselling, loan, sub-licensing, systematic supply, or distribution in any form to anyone is expressly forbidden. Terms & Conditions of access and use can be found at <http://www.tandfonline.com/page/terms-and-conditions>

Theoretical and experimental analysis of subwavelength bowtie-shaped antennas

Arif E. Cetin^{a,b,c,d}, Serap Aksu^{e,f}, Mustafa Turkmen^{a,g,*}, Dordaneh Etezadi^{a,b} and Hatice Altug^b

^aDepartment of Electrical and Computer Engineering, Boston University, Boston, MA 02215, USA; ^bBioengineering Department, EPFL, Lausanne CH-1015, Switzerland; ^cDepartment of Biological Engineering, Massachusetts Institute of Technology, Cambridge, MA 02139, USA; ^dKoch Institute for Integrative Cancer Research, Massachusetts Institute of Technology, Cambridge, MA 02139, USA; ^eDivision of Materials Science and Engineering, Boston University, Boston, MA 02215, USA; ^fDepartment of Biosystems Science and Engineering, ETH Zürich, Basel 4058, Switzerland; ^gDepartment of Electrical and Electronics Engineering, Erciyes University, Kayseri 38039, Turkey

(Received 13 October 2014; accepted 10 May 2015)

Recently, bowtie-shaped apertures have received significant attention due to their extraordinary ability to generate dramatic field enhancement and light confinement in nanometer scale. In this article, we investigate both experimentally and theoretically nearfield and farfield responses of bowtie-shaped apertures in detail. We study the role of bowtie gap in creating large and highly accessible local electromagnetic fields. In order to experimentally excite strong local fields, we introduce a high-resolution and lift-off free fabrication method which enables bowtie apertures with gap sizes down to sub-10 nm. We also show that for identical geometries, bowtie-shaped apertures support much stronger local electromagnetic fields compared to particle-based bowtie-shaped antennas. We investigate the role of polarization on the gap effect, which plays the dominant role for creating strong nearfield intensities. Finally, we introduce a mechanism to fine-tune the optical response of bowtie apertures through geometrical parameters.

1. Introduction

Confinement of light on subwavelength scales with large local fields by exploitation of surface plasmons, which are collective charge oscillations, leads the demonstration of revolutionary concepts, i.e. nearfield optical microscopy,[1–3] high-density data storage, [4,5] nanolithography,[6–8] label-free biosensing,[9–13] and surface-enhanced vibrational spectroscopy.[14–21] In this regard, subwavelength apertures through thin metal films received significant attention due to their ability to create nearfield enhancements and light confinement in nanometer scale.[16,22] Compared to conventional optical systems, i.e. mirrors and lenses suffering from diffraction limit, plasmonic nanoapertures with different shapes and sizes provide a convenient way for controlling light.[23,24] Consequently, isolated apertures have been offered for light confinement applications.[25] However, these apertures suffer from weak light transmission due to the low efficiency of evanescent tunneling in the absence of a collective array

*Corresponding author. Email: turkmen@erciyes.edu.tr

behavior.[26–28] Here, the transmission is associated with only the excitation of localized surface plasmons. Light transmission can be enhanced by one order of magnitude using subwavelength circular aperture arrays. Here, the grating lattice of the periodic array overcomes the momentum mismatch between surface plasmons and the incident light, which enables the excitation of propagating surface plasmons. Light is then coupled through the apertures by the evanescent tunneling effect, and the surface plasmons are excited at the aperture exit while scattered into a transmitted light.[29,30] Transmission can be further enhanced by periodic rectangular aperture arrays, where the constituting aperture elements support propagating modes induced by the polarization of the illumination source, enabling the apertures to behave like a waveguide.[31,32] Ridge apertures, such as C- and H-shaped nanoholes, can increase the transmission further thanks to their open arms which allow light to propagate through the openings.[33,34] Their high transmittance is related to the collective effect of the waveguide modes and the propagating surface plasmons excited within the aperture.[33–35] However, these apertures suffer from weak nearfield intensities as the transmitted light diffracts at the aperture exit rather than focus. In order to address this issue, recently bowtie-shaped antennas have been introduced as the local electromagnetic fields can be significantly enhanced within the nanoscale gap, which allows the excitation of highly confined localized surface plasmons, while preserving the transmission quality.[35–38]

In this study, we both experimentally and theoretically investigate nearfield and far-field characteristics of bowtie-shaped nanoapertures in detail. We first determine the dependence of the nearfield enhancements on bowtie gap. Then, we show the effect of polarization on the excitation of local electromagnetic fields within the gap region. Finally, we quantitatively demonstrate the dependence of the farfield transmission response on the aperture geometry. For the experimental demonstration, we utilize a lift-off free and high-resolution fabrication scheme, which enables the realization of bowtie gaps down to sub-10 nm. Figure 1(a) shows the illustration of the bowtie-shaped apertures with the geometrical parameters: θ = tip angle, L = hemline length, H = height, G = gap width, D = bottom edge-to-edge distance between two bowtie apertures, and P = period of the array. Figure 1(b) shows the scanning electron microscopy (SEM) image of the fabricated bowtie-shaped aperture with 20 nm gap.

2. Fabrication of bowtie-shaped apertures

For experimental demonstration, we fabricate free-standing bowtie-shaped apertures on a thin silicon nitride membrane by a high-resolution and lift-off free fabrication technique.

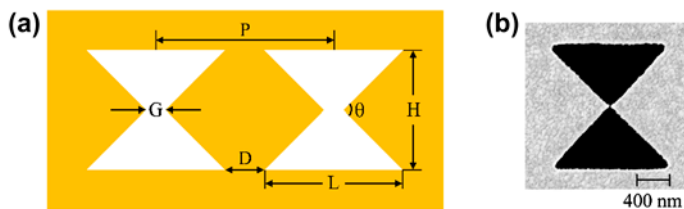


Figure 1. (a) Schematic illustration of the bowtie-shaped aperture array indicating the geometrical parameters and (b) SEM image of the fabricated aperture with 20 nm gap. Corresponding device parameters are as follows: $\theta = 90^\circ$, $L = 1450$ nm, $H = 1430$ nm, $D = 450$ nm, and $P = 1900$ nm.

Steps of the fabrication process are schematically illustrated in Figure 2(a).[39–41] We use a 500- μm silicon wafer with 80 nm low pressure chemically deposited silicon nitride film on both sides. (i) Membrane patterns, with a size of 750 $\mu\text{m} \times 750 \mu\text{m}$, are created by photolithography (SUSS MicroTec MA/BA6 Mask Aligner) performed on a 2- μm photoresist (MICROPOSITTM S1818TM) on the bottom silicon nitride film. After development, silicon nitride layers within the transferred patterns are removed via dry etching (Plasma Therm 790 RIE/PECVD System) with SF_6 and He gases. (ii) The wafer is then immersed in a KOH solution for wet etching in order to realize free-standing silicon nitride membranes. (iii) Bowtie-shaped patterns are created by electron-beam lithography (Zeiss Supra 40) on a positive resist (polymethyl methacrylate, PMMA). Apertures are created by dry etching with SF_6 and Ar gases while PMMA is used as a mask. Oxygen plasma is later performed (PVA TePla America) to remove the remaining residues on the silicon nitride surface. (iv) Finally, we deposit 5 nm titanium as an adhesion layer and 100 nm gold (CHA SolutionTM) realizing plasmonic bowtie-shaped apertures in a lift-off free manner. Figure 2(b) shows the bowtie arrays demonstrating the fabricated apertures are well defined and uniform over large areas. Our high-resolution nanomanufacturing technique enables us to fabricate variety of bowtie apertures with different gap sizes down to sub-10 nm (Figure 2(c)). These small gap formations generate large local electromagnetic fields, which is highly crucial for applications demanding strong sensitivities to surface conditions.

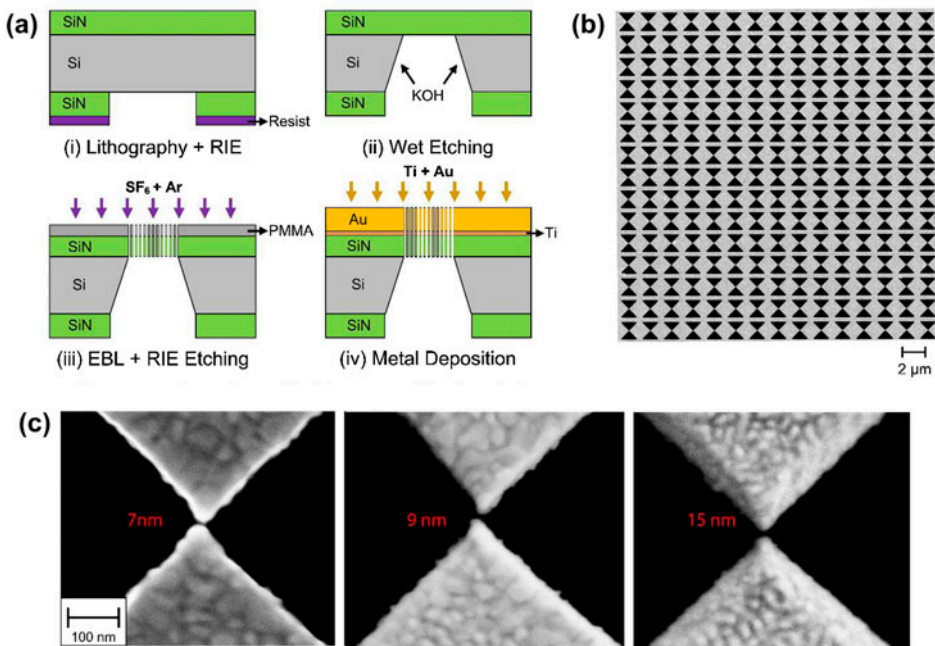


Figure 2. (a) High-resolution and lift-off free fabrication method for bowtie-shaped apertures based on electron-beam lithography and (b) SEM image of the fabricated bowtie array with 20 nm gap. Device parameters are as follows: $\theta = 90^\circ$, $L = 1450 \text{ nm}$, $H = 1430 \text{ nm}$, $D = 450 \text{ nm}$, and $P = 1900 \text{ nm}$. Thicknesses of the gold and silicon nitride (SiN) layers are 100 and 80 nm, respectively and (c) SEM images of the fabricated bowtie-shaped apertures with different gap sizes: 7, 9, and 15 nm. Corresponding device parameters are as follows: $\theta = 90^\circ$, $L = 1450 \text{ nm}$, $H = L - M$, and $P = 1900 \text{ nm}$.

Farfield and nearfield characteristics of the bowtie-shaped apertures strongly depend on the geometrical parameters and the polarization direction of the illumination source.[42] In the following sections, we will investigate the effects of these parameters on bowtie response in detail.

3. Gap effect on nearfield response

Rectangular apertures support different modes depending on the polarization direction of the illumination source.[28] They support propagating modes when polarization is along the x -direction (parallel to the short axis of the aperture) while significantly attenuate the y -polarized source (perpendicular to the short axis of the aperture).[30] Hence, light transmission is negligible for y -polarization (not shown here). In order to highlight the effect of the gap on farfield response, we compare the transmissivity of rectangular and bowtie-shaped apertures with identical aperture areas, S as schematically illustrated in Figure 3(a). The apertures are with the same height ($H = dy$) and different lengths ($L \neq dx$). Here, transmissivity is defined as the ratio between the transmitted photons from the aperture system and the expected transmitted photons calculated from the conventional transmission theory: Transmissivity = Transmission \times (Period²/Aperture Area). Here, we compare transmissivity instead of transmission in order to consider the

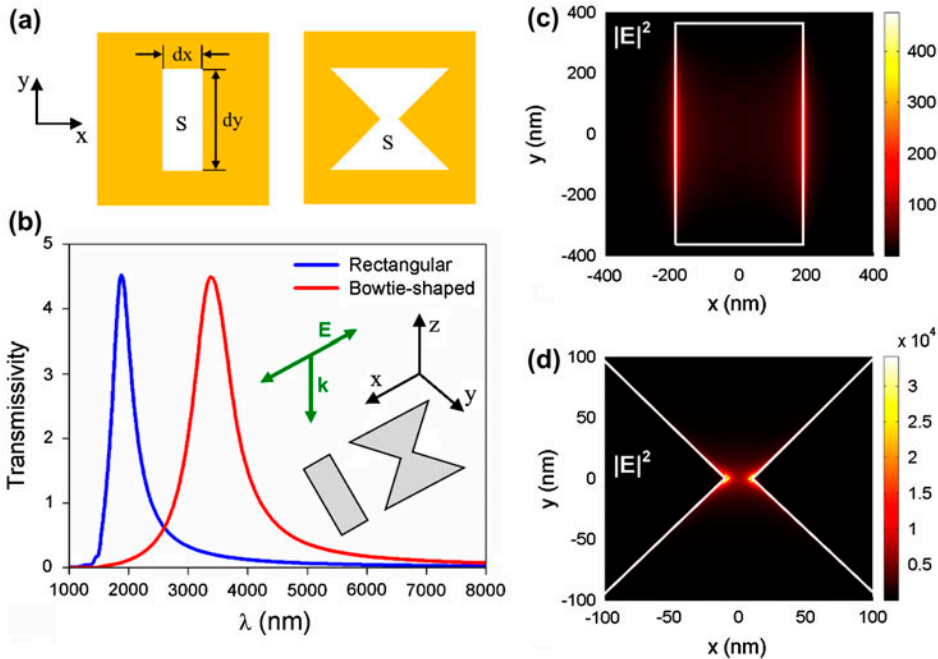


Figure 3. (a) Schematic illustration of the rectangular and the bowtie-shaped apertures with the same opening area, S and (b) calculated transmissivities of rectangular (blue curve) and bowtie-shaped (red curve) apertures. In figure inset, propagation and polarization directions of the illumination source are illustrated with green arrows. Nearfield intensity enhancement distributions ($|E|^2$) are calculated at the top surface of the gold layer for (c) rectangular ($\lambda_{res} = 1849$ nm) and (d) bowtie-shaped apertures ($\lambda_{res} = 3311$ nm). Corresponding device parameters are as follows: (i) for rectangular aperture, $dx = 385$ nm and $dy = 730$ nm, (ii) for bowtie-shaped aperture, $\theta = 90^\circ$, $L = 750$ nm, $H = 730$ nm, $G = 20$ nm, $D = 450$ nm, and $P = 1200$ nm.

transmission differences due to variations in the aperture opening areas. For numerical analyses on nearfield and farfield, we perform finite difference time domain simulations using Lumerical Solutions, Inc. In simulations, dielectric constants of materials are taken from Ref. [43]. For the unit cell consisting of a single aperture, periodic boundary condition is used along x - and y -axes to create the periodic array behavior and perfectly matched layer boundary condition is used along z -axis. Figure 3(b) shows that the two apertures have similar transmissivity in magnitude, while the resonance wavelength of the rectangular aperture (blue curve) is in shorter wavelength ($\lambda_{\text{res}} = 1849$ nm) compared to that of the bowtie-shaped aperture (red curve, $\lambda_{\text{res}} = 3311$ nm) under an x -polarized light source. Rectangular aperture supports a sharper resonance, with linewidth 369 nm vs. 729 nm, but it significantly suffers from nearfield enhancements. Figure 3(c) and (d) shows the nearfield intensity enhancement distributions calculated at the top surface of the metal layer, demonstrating that the bowtie aperture supports two orders of magnitude ($|E|^2 = 35,000$) larger nearfield intensity enhancement compared to the rectangular aperture ($|E|^2 = 450$) with the same opening area.

This nearfield enhancement can be further amplified using smaller gaps.[42] As shown in Figure 4(a), reducing the gap from 20 to 10 nm, nearfield intensity enhancement is twofold improved ($|E|^2 = 65,000$). As shown in the cross-sectional field profile (Figure 4(b)), local electromagnetic fields with high enhancements are mainly concentrated along the metal wall and support similar nearfield distributions at xy -plane with minor variations in the enhancement values.

4. Bowtie aperture vs. bowtie antenna

Particle-based bowtie-shaped antennas are utilized in applications which demand large nearfield enhancements.[44–49] In this section, we demonstrate that these nearfield enhancements can be further amplified by bowtie-shaped apertures. Figure 5(a) illustrates the bowtie-shaped antenna complementary to the bowtie-shaped aperture with 20 nm gap. Height of the bowtie antenna is identical to the thickness of the metal layer forming the bowtie aperture (100 nm). Here, the resonance wavelength of the antenna (not shown here) is observed in shorter wavelengths ($\lambda_{\text{res}} = 1930$ nm) compared to that

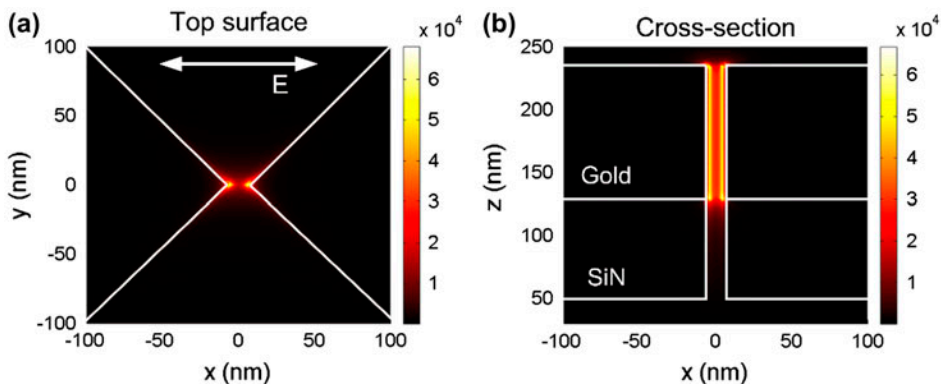


Figure 4. Nearfield intensity enhancement distributions ($|E|^2$) calculated (a) at the top surface of the metal layer and (b) through cross section for the bowtie-shaped aperture with 10 nm gap at $\lambda_{\text{res}} = 3556$ nm. Polarization direction is indicated with a white arrow. Corresponding device parameters are as follows: $\theta = 90^\circ$, $L = 750$ nm, $H = 730$ nm, $D = 450$ nm, and $P = 1200$ nm.

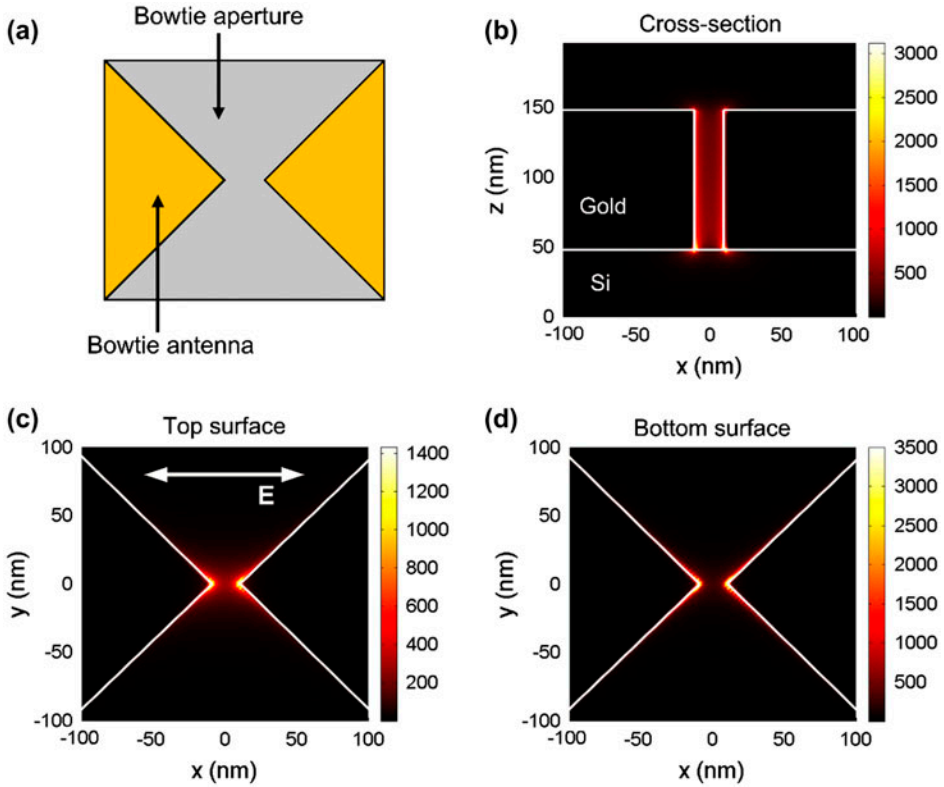


Figure 5. (a) Schematic view of the bowtie-shaped aperture and the complementary particle-based bowtie-shaped antenna. Nearfield intensity enhancement distribution ($|E|^2$) is calculated for the bowtie-shaped antenna at $\lambda_{\text{res}} = 1930$ nm, (b) through cross section and at (c) top and (d) bottom surfaces of the antenna. Polarization direction is indicated with a white arrow. Corresponding device parameters are: $\theta = 90^\circ$, $G = 20$ nm, $L = 750$ nm, $H = 730$ nm, $D = 450$ nm, and $P = 1200$ nm.

of the aperture ($\lambda_{\text{res}} = 3311$ nm). Figure 5(b) shows that the bowtie-shaped antenna shows an order of magnitude smaller nearfield intensity enhancement ($|E|^2 = 3000$) compared to the bowtie-shaped aperture. Furthermore for the bowtie-shaped aperture, highly enhanced local fields preserve their intensities within the gap region (Figure 4(b)), while for the bowtie-shaped antenna, they are mainly concentrated at the gold/dielectric interface and their intensities decrease along the z -direction. For example, the antenna supports more than two times larger nearfield intensity enhancement at the gold/silicon interface (bottom antenna surface in Figure 5(d)) than at the air/gold interface (top antenna surface in Figure 5(c)). Hence, bowtie-shaped apertures are more advantageous than bowtie-shaped antennas for applications demanding strong surface enhancements as they support much larger local electromagnetic fields which expand over a wider sensing surface.

5. Dependence on the polarization

For an x -polarized light source in addition to localized surface plasmons excited within the gap region, bowtie-shaped apertures support propagating waveguide modes,

which enhance both light transmission and nearfield enhancements further. For a y -polarized light source, bowtie gap provides a coupling between two triangle shaped apertures, which enhances the optical transmission. As a result, aperture system can still exhibit high transmissivity.[28] For instance, Figure 6(a) shows the bowtie transmissivity for x - (blue curve) and y -polarized (red curve) illumination sources, demonstrating similar transmissivity values for different polarizations, while the transmission resonance for y -polarized source is observed in shorter wavelengths ($\lambda_{\text{res}} = 1454$ nm) compared to the one for x -polarized one ($\lambda_{\text{res}} = 3311$ nm). Furthermore, y -polarization supports sharper resonances, with linewidths 351 nm vs. 774 nm. However, the lack of localized surface plasmon excitations and waveguide modes due to the absence of the gap effect results in weaker local electromagnetic fields. For the y -polarized light source (Figure 6(a)-inset), rather than collimating around the tip region, transmitted light is concentrated at the upper and lower walls. Hence, the system is not able to exploit the gap effect and supports 2 orders of magnitude lower nearfield intensity enhancements ($|E|^2 = 300$) compared to x -polarized light source ($|E|^2 = 35,000$).

For the experimental demonstration, we compare the farfield responses of the bowtie-shaped apertures with 100 nm gap for different polarizations through Fourier transform infrared (FTIR) microscopy. Experimental setup consists of an IR-microscope coupled to a Bruker FTIR spectrometer with a KBr beam splitter. Light is illuminated normally, and the transmitted signal is collected by a Cassagrian optics, coupled into a liquid N_2 -cooled mercury cadmium telluride detector. Figure 6(b) demonstrates the good correlation between experimental (dashed curves) and numerical (solid curves) results. As expected for the y -polarized light source, resonance wavelength is observed in shorter wavelengths with smaller linewidths compared to x -polarized source.

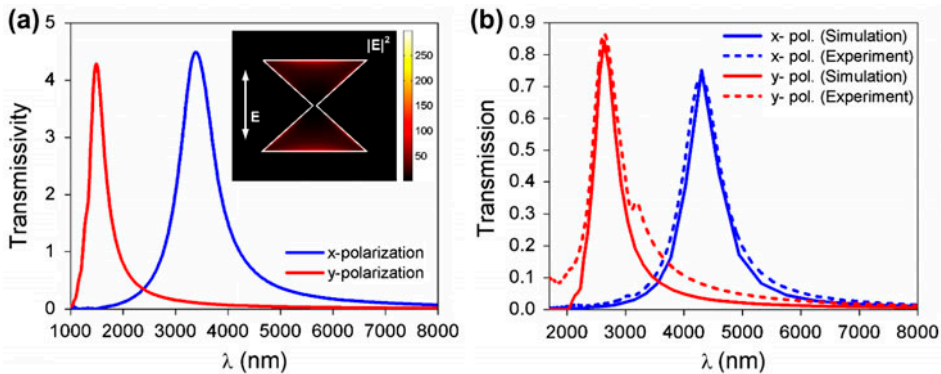


Figure 6. (a) Calculated transmissivity for x - (blue curve) and y -polarized (red curve) illumination sources. Figure inset: nearfield intensity enhancement distribution ($|E|^2$) calculated at $\lambda_{\text{res}} = 1454$ nm for y -polarized incident light (Polarization direction is indicated with a white arrow.). Corresponding device parameters are as follows: $\theta = 90^\circ$, $L = 750$ nm, $H = 730$ nm, $G = 20$ nm, $D = 450$ nm, and $P = 1200$ nm. (b) Experimental (dashed curves) and calculated (solid curves) transmission responses for x - (blue curves) and y -polarized (red curves) light sources. Corresponding device parameters are as follows: $\theta = 90^\circ$, $G = 20$ nm, $D = 450$ nm, $L = P - D$, and $H = (L - G) \times \tan(\theta/2)$.

6. Dependence on the device parameters

In this section, we investigate the dependence of the bowtie farfield response on the geometrical device parameters: gap width (G), tip angle (θ), and perimeter (Per.).

6.1. Gap width (G)

In Figure 7(a), we show the resonance wavelength, λ_{res} for different bowtie gaps where the hemline length (L) and the height (H) of the aperture are fixed at 750 and 730 nm, respectively, while the tip angle (θ) is varied by changing the sidewalls as illustrated in the figure inset. The transmission resonance shifts to shorter wavelengths for the wider gaps.[22,42,50] This behavior can be simply explained using an analogy with dipole-dipole interactions.[51] For an x -polarized light source, bowtie tips are polarized where the charges at the crossing tips create an attractive force which lowers the plasmon energy. Consequently, for the wider gap width, this effect diminishes such that the plasmon energy increases and the transmission resonance shifts to shorter wavelengths. Here, we determine a quadratic relationship between resonance wavelength and bowtie gap (red curve), $\lambda_{\text{res}} = 0.033 \times G^2 - 11.2 \times G + \text{Const}$.

We then investigate this relationship, where the gap width is varied by changing the height while the tip angle ($\theta = 90^\circ$) and the hemline length ($L = 750$ nm) are fixed. As shown in Figure 7(b), resonance wavelength has a similar quadratic relationship with bowtie gap, $\lambda_{\text{res}} = 0.036 \times G^2 - 13.6 \times G + \text{Const}$.

6.2. Tip angle (θ)

In Figure 8(a), we first vary height while keeping the hemline length constant ($L = 750$ nm). As the tip angle decreases from $\theta = 90^\circ$ to $\theta = 50^\circ$, transmission resonance shifts to shorter wavelengths and gets narrower. We obtain a linear relationship between resonance wavelength and perimeter of the bowtie-shaped aperture, $\lambda_{\text{res}} = 1.9 \times \text{Per.} + \text{Const}$. Here, making the tip angle smaller amplifies both nearfield intensity (not shown here) and transmissivity. However, further minimizing the tip

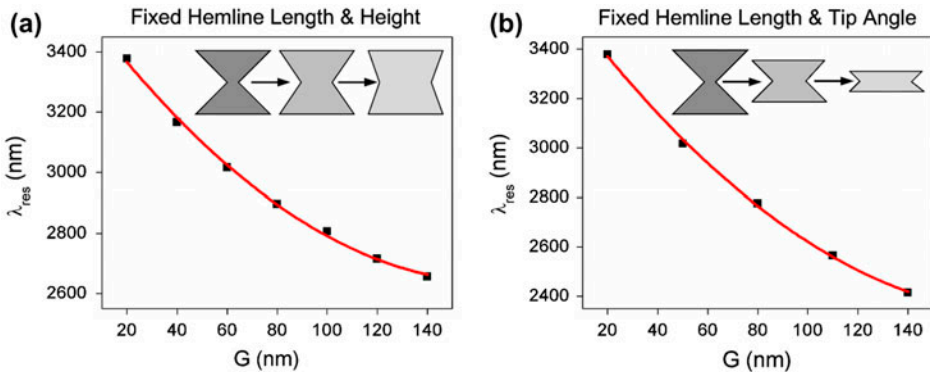


Figure 7. (a) Calculated resonance wavelength (λ_{res}) for different bowtie gaps: (a) L (=750 nm) and H (=730 nm) are fixed while θ is varied, where $D = 450$ nm, $P = 1200$ nm and (b) L (=750 nm) and θ (=90°) are fixed while H is varied, where $H = L - G$, $D = 450$ nm, $P = 1200$ nm. In figure insets, gap variation procedures are illustrated.

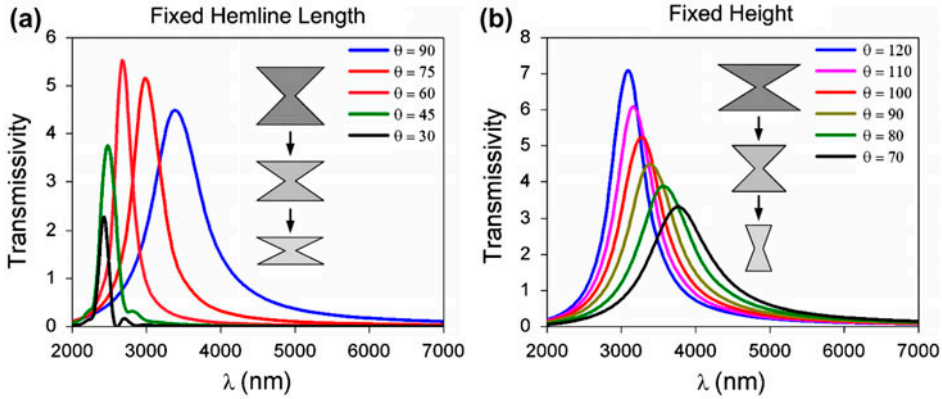


Figure 8. Calculated transmissivity for different tip angles, where (a) H is varied and L is fixed. Corresponding device parameters are as follows: $G = 20$ nm, $L = 750$ nm, $H = 730 \times \tan(\theta/2)$, $D = 450$ nm and $P = 1200$ nm, and (b) L is varied and H is fixed. Corresponding device parameters are as follows: $G = 20$ nm, $H = 730$ nm, $L = 20 + 730/\tan(\theta/2)$, $D = P - L$ and $P = 1200$ nm. In figure insets, tip angle variation procedures are illustrated.

angle (below $\theta = 50^\circ$), transmissivity dramatically diminishes since the open arms of the aperture become smaller such that the bowtie system is not able to allow light to propagate through it.

Second, we vary the tip angle by changing the hemline length while keeping the height constant ($H = 730$ nm) as shown in Figure 8(b). For wider tip angles, transmission resonance shifts to shorter wavelengths and gets narrower, while transmissivity increases. Similarly, resonance wavelength has a linear relationship with bowtie perimeter, $\lambda_{\text{res}} = 1.1 \times \text{Per.} + \text{Const.}$ Here, making the tip angle larger increases both nearfield intensity (not shown here) and transmissivity.

6.3. Perimeter (Per.)

In this section, we investigate the effect of the bowtie perimeter on the farfield response by resizing the whole aperture geometry. First, we keep the distance between two bowtie apertures constant at $D = 450$ nm and resize the apertures by varying the hemline length and height while fixing the tip angle at $\theta = 90^\circ$. As shown in Figure 9(a) for larger apertures, transmission resonance shifts to longer wavelengths and gets broader while transmissivity decreases. For different D values (450, 500, 600, and 1000 nm), we obtain a linear relationship between resonance wavelength and bowtie perimeter, $\lambda_{\text{res}} = 0.81 \times \text{Per.} + C_i$ where C_i is constant. We investigate this relationship for different tip angles at $D = 450$ nm for gap sizes 20 and 60 nm. At $G = 20$ nm, for tip angles $\theta = 45^\circ$, 60° , 90° , and 100° , we determine a linear relationship, $\lambda_{\text{res}} = 0.59 \times \text{Per.} + 640$, $\lambda_{\text{res}} = 0.65 \times \text{Per.} + 610$, $\lambda_{\text{res}} = 0.81 \times \text{Per.} + 500$, and $\lambda_{\text{res}} = 0.88 \times \text{Per.} + 460$, respectively. Similarly, for $G = 60$ nm, we obtain $\lambda_{\text{res}} = 0.55 \times \text{Per.} + 550$, $\lambda_{\text{res}} = 0.61 \times \text{Per.} + 450$, $\lambda_{\text{res}} = 0.74 \times \text{Per.} + 350$, and $\lambda_{\text{res}} = 0.83 \times \text{Per.} + 230$. These results demonstrate that for the apertures with different gaps, slope of the linear function decreases and constant in the function increases with smaller tip angles, while for the apertures with different tip angles, slope and constant in the linear function decrease with larger gap widths.

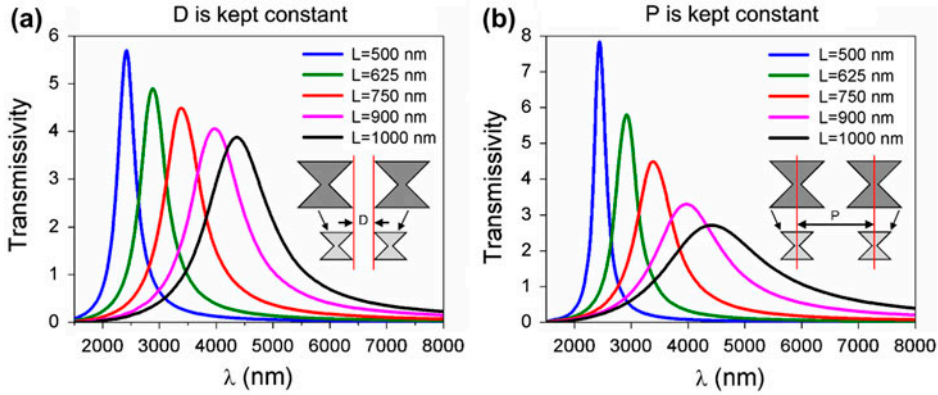


Figure 9. Calculated transmissivity for different perimeters where H and L are varied while ($=90^\circ$) and G ($=20$ nm) are kept constant via: (a) varying period ($P=L+450$) for fixed $D=450$ nm and (b) varying D ($D=1200-L$) for fixed $P=1200$ nm. In figure inset, perimeter variation procedures are illustrated.

Second, we keep periodicity constant at $P=1200$ nm and resize the apertures as above. As shown in Figure 9(b) for larger apertures, transmission resonance shifts to longer wavelengths and gets broader while transmissivity decreases. For different P values, 1200, 1300, 1400, and 2400 nm, resonance wavelength has a linear relationship with bowtie perimeter, $\lambda_{\text{res}} = 0.81 \times \text{Per.} + C_i$ where C_i is constant. We investigate perimeter effect on bowtie aperture with gap sizes 20 and 60 nm at $P=1200$ nm. At $G=20$ nm, linear relationships for $\theta=45^\circ, 60^\circ, 90^\circ$, and 100° are $\lambda_{\text{res}} = 0.58 \times \text{Per.} + 680$, $\lambda_{\text{res}} = 0.62 \times \text{Per.} + 650$, $\lambda_{\text{res}} = 0.81 \times \text{Per.} + 530$, and $\lambda_{\text{res}} = 0.88 \times \text{Per.} + 470$, respectively. Similarly, for $G=60$ nm, we obtain $\lambda_{\text{res}} = 0.51 \times \text{Per.} + 600$, $\lambda_{\text{res}} = 0.56 \times \text{Per.} + 590$, $\lambda_{\text{res}} = 0.72 \times \text{Per.} + 430$, and $\lambda_{\text{res}} = 0.78 \times \text{Per.} + 380$. These results demonstrate that for the apertures with different gaps, slope of the linear function diminishes and the constant in the function increases

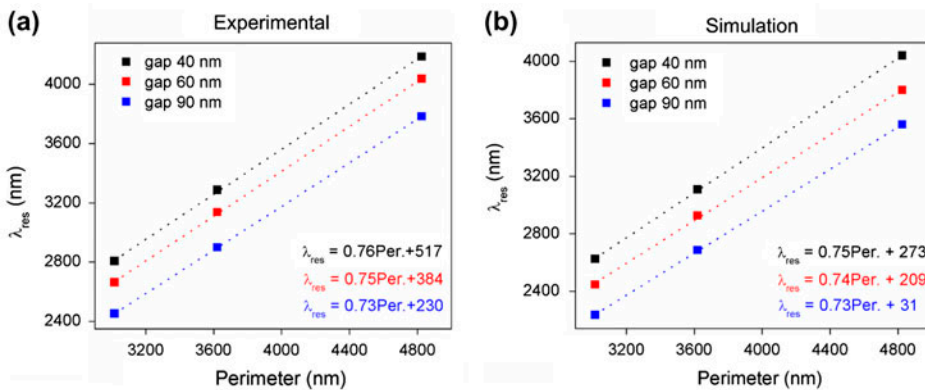


Figure 10. (a) Experimental and (b) calculated linear relationships between resonance wavelength (λ_{res}) and perimeter (Per.) of the bowtie-shaped apertures with different gaps. Corresponding device parameters are as follows: $\theta=90^\circ$, $L=1450$ nm, $H=L-G$, and $P=1900$ nm.

with smaller tip angles, while for the apertures with different tip angles, slope and constant in the linear function decrease with larger gap widths.

In order to experimentally investigate the relationship between resonance wavelength (λ_{res}) and the perimeter (Per.), we fabricate bowtie apertures with different gaps. Figure 10(a) and (b) shows the experimental and numerical results demonstrating their good agreement. For the gaps sizes, 40, 60, and 90 nm, we experimentally (numerically) obtain linear relationships, $\lambda_{\text{res}} = 0.76 \times \text{Per.} + 517$ ($\lambda_{\text{res}} = 0.75 \times \text{Per.} + 273$), $\lambda_{\text{res}} = 0.75 \times \text{Per.} + 384$ ($\lambda_{\text{res}} = 0.74 \times \text{Per.} + 209$), $\lambda_{\text{res}} = 0.73 \times \text{Per.} + 230$ ($\lambda_{\text{res}} = 0.73 \times \text{Per.} + 31$). Rectangular nanorod antennas show a similar linear relationship, where resonance wavelength is linearly proportional to rod length, L , $\lambda_{\text{res}} = 2 \times n_{\text{eff}} \times L$ where n_{eff} is the effective refractive index accounting for the inhomogeneous dielectric environment surrounding the antenna.[52–54] Here, resonances observed in the spectrum correspond to surface plasmon excitations triggered by the electric field of light. In the case of rectangular antennas, resonance wavelength is proportional to the effective oscillation path length of the conduction electrons which is the length of the nanorod antenna.[52,53] On the other hand for bowtie-shaped apertures, these conduction electrons mainly concentrate at the aperture edge.[53] Therefore, resonance wavelength has a linear relationship with the perimeter, $\lambda_{\text{res}} = a \times \text{Per.} + c$ where slope and constant of the function depend on the device parameters as well as the materials composing the aperture.

7. Conclusion

In conclusion, we experimentally and numerically investigate nearfield and farfield properties of bowtie-shaped apertures. We demonstrate that the aperture system with small gaps support highly enhanced local electromagnetic fields. In order to realize small gap features, we introduce a high-resolution and lift-off free fabrication method. We also show that bowtie-shaped apertures support much higher nearfield intensity enhancements compared to particle-based bowtie-shaped antennas. Furthermore, we investigate the dependence of the nearfield resolution on polarization direction of the incident light source. Finally, we introduce a fine-tuning mechanism for controlling the farfield response through device parameters in order to realize aperture systems working in the desired wavelengths.

Acknowledgement

Authors acknowledge the Technological Research Council of Turkey (TUBITAK) under research grants 113E277. Altug Research Group acknowledges Ecole Polytechnique Federale de Lausanne (EPFL).

References

- [1] Kalkbrenner T, Håkanson U, Schädle A, et al. Optical microscopy via spectral modifications of a nanoantenna. *Phys. Rev. Lett.* 2005;95:200801-1–200801-4.
- [2] Sánchez EJ, Novotny L, Xie XS. Near-field fluorescence microscopy based on two-photon excitation with metal tips. *Phys. Rev. Lett.* 1999;82:4014–4017.
- [3] Zhang Z, Ahn P, Dong B, et al. Quantitative imaging of rapidly decaying evanescent fields using plasmonic near-field scanning optical microscopy. *Sci. Rep.* 2013;3:2803-1–2803-8.
- [4] Betzig E, Trautman JK, Wolfe R, et al. Near-field magneto-optics and high density data storage. *Appl. Phys. Lett.* 1992;61:142–144.

- [5] Park S, Hahn JW. Plasmonic data storage medium with metallic nano-aperture array embedded in dielectric material. *Opt. Exp.* 2009;17:20203–20210.
- [6] Liu Z, Wei Q, Zhang X. Surface plasmon interference nanolithography. *Nano Lett.* 2005;5:957–961.
- [7] Aksu S, Cetin AE, Adato R, et al. Plasmonically enhanced vibrational biospectroscopy using low-cost infrared antenna arrays by nanostencil lithography. *Adv. Opt. Mater.* 2013;1:798–803.
- [8] Guo X, Du J, Guo Y, et al. Large-area surface-plasmon polariton interference lithography. *Opt. Lett.* 2006;31:2613–2615.
- [9] Yanik AA, Huang M, Kamohara O, et al. An optofluidic nanoplasmonic biosensor for direct detection of live viruses from biological media. *Nano Lett.* 2010;10:4962–4969.
- [10] Yanik AA, Cetin AE, Huang M, et al. Seeing protein monolayers with naked eye through plasmonic Fano resonances. *Proc. Natl. Acad. Sci. USA.* 2011;108:11784–11789.
- [11] Cetin AE, Altug H. Fano resonant ring/disk plasmonic nanocavities on conducting substrates for advanced biosensing. *ACS Nano.* 2012;6:9989–9995.
- [12] Coskun AF, Cetin AE, Galarreta BC, et al. Lensfree optofluidic plasmonic sensor for real-time and label-free monitoring of molecular binding events over a wide field-of-view. *Sci. Rep.* 2014;4:1–7.
- [13] Cetin AE, Coskun AF, Galarreta BC, et al. Handheld high-throughput plasmonic biosensor using computational on-chip imaging. *Light. Sci. Appl.* 2014;3:1–10.
- [14] Adato R, Yanik AA, Amsden JJ, et al. Ultra-sensitive vibrational spectroscopy of protein monolayers with plasmonic nanoantenna arrays. *Proc. Natl. Acad. Sci. USA.* 2009;106:19227–19232.
- [15] Cetin AE, Yanik AA, Yilmaz C, et al. Monopole antenna arrays for optical trapping, spectroscopy and sensing. *Appl. Phys. Lett.* 2011;98:111110-1–111110-3.
- [16] Wu CW, Khanikaev AB, Adato R, et al. Fano-resonant asymmetric metamaterials for ultrasensitive spectroscopy and identification of molecular monolayers. *Nat. Mater.* 2012;11:69–75.
- [17] Cetin AE, Etezadi D, Altug H. Accessible nearfields by nanoantennas on nanopedestals for ultrasensitive vibrational spectroscopy. *Adv. Opt. Mater.* 2014;2:866–872.
- [18] Cetin AE, Turkmen M, Aksu S, et al. Multi-resonant compact nanoaperture with accessible large nearfields. *Appl. Phys. B.* 2015;118:29–38.
- [19] Turkmen M. Characterization of x-shaped nanoaperture antenna arrays operating in mid-infrared regime. *Chin. Opt. Lett.* 2013;11:070501-1–070501-4.
- [20] Sendur K, Challener W. Near-field radiation of bow-tie antennas and apertures at optical frequencies. *J. Microsc.* 2002;210:279–283.
- [21] Adato R, Yanik AA, Wu C-H, et al. Radiative engineering of plasmon lifetimes in embedded nanoantenna arrays. *Opt. Exp.* 2010;18:4526–4537.
- [22] Schuck PJ, Fromm DP, Sundaramurthy A, et al. Improving the mismatch between light and nanoscale objects with gold bowtie nanoantennas. *Phys. Rev. Lett.* 2005;94:017402-1–017402-4.
- [23] Muhlschlegel P, Eisler HJ, Martin OJF, et al. Resonant optical antennas. *Science.* 2005;308:1607–1609.
- [24] Shi X, Hesselink L, Thornton RL. Ultrahigh light transmission through a C-shaped nanoaperture. *Opt. Lett.* 2003;28:1320–13226.
- [25] Shi X, Hesselink L. Mechanisms for enhancing power throughput from planar nano-apertures for near-field optical data storage. *Jpn. J. Appl. Phys.* 2002;41:1632–1635.
- [26] Bethe HA. Theory of diffraction by small holes. *Phys. Rev.* 1944;66:163–182.
- [27] Chang S-H, Gray S, Schatz G. Surface plasmon generation and light transmission by isolated nanoholes and arrays of nanoholes in thin metal films. *Opt. Exp.* 2005;13:3150–3165.
- [28] Jin EX, Xu X. Plasmonic effects in near-field optical transmission enhancement through a single bowtie-shaped aperture. *Appl. Phys. B.* 2006;84:3–9.
- [29] Darmanyan S, Zayats A. Light tunneling via resonant surface plasmon polariton states and the enhanced transmission of periodically nanostructured metal films: an analytical study. *Phys. Rev. B.* 2003;67:035424-1–035424-7.
- [30] Lezec H, Thio T. Diffracted evanescent wave model for enhanced and suppressed optical transmission through subwavelength hole arrays. *Opt. Exp.* 2004;12:3629–3651.

- [31] Koerkamp JK, Enoch S, Segerink FB, et al. Strong influence of hole shape on extraordinary transmission through periodic arrays of subwavelength holes. *Phys. Rev. Lett.* 2004;92:183901-1–183901-4.
- [32] Degiron A, Ebbesen TW. The role of localized surface plasmon modes in the enhanced transmission of periodic subwavelength apertures. *J. Opt. A: Pure Appl. Opt.* 2005;7:S90–S96.
- [33] Itagi AV, Stancil DD, Bain JA, et al. Ridge waveguide as a near-field optical source. *Appl. Phys. Lett.* 2003;83:4474–4476.
- [34] Jin EX, Xu X. Finitte-difference time-domain studies on optical transmission through planar nano-apertures in a metal film. *Jpn. J. Appl. Phys.* 2004;43:407–417.
- [35] Jin EX, Xu X. Enhanced optical near field from a bowtie aperture. *Appl. Phys. Lett.* 2006;88:153110-1–153110-3.
- [36] Oh S, Lee T, Hahn JW. Multifunctional bowtie-shaped ridge aperture for overlay alignment in plasmonic direct writing lithography using a contact probe. *Opt. Lett.* 2013;38:2250–2252.
- [37] Cubukcu E, Kort EA, Crozier KB, et al. Plasmonic laser antenna. *Appl. Phys. Lett.* 2006;89:093120-1–093120-3.
- [38] Dalir H, Koyama F. High-speed operation of bow-tie-shaped oxide aperture VCSELs with photon–photon resonance. *Appl. Phys. Exp.* 2014;7:022102-1–022102-4.
- [39] Yanik AA, Huang M, Artar A, et al. Integrated nanoplasmonic-nanofluidic biosensors with targeted delivery of analytes. *Appl. Phys. Lett.* 2010;96:021101-1–021101-3.
- [40] Aksu S, Yanik AA, Adato R, et al. High-throughput nanofabrication of infrared plasmonic nanoantenna arrays for vibrational nanospectroscopy. *Nano. Lett.* 2010;10:2511–2518.
- [41] Turkmen M, Aksu S, Çetin AE, et al. Multi-resonant metamaterials based on UT-shaped nano-aperture antennas. *Opt. Exp.* 2011;19:7921–7928.
- [42] Dittlacher H, Krenn JR, Felidj N, et al. Fluorescence imaging of surface plasmon fields. *Appl. Phys. Lett.* 2001;80:404–406.
- [43] Palik ED. *Handbook of optical constants of solids*. Orlando, FL: Academic; 1985.
- [44] Yu N, Cubukcu E, Diehl L, et al. Bowtie plasmonic quantum cascade laser antenna. *Opt. Exp.* 2007;15:13272–13281.
- [45] Sederberg S, Elezzabi AY. Sierpiński fractal plasmonic antenna: a fractal abstraction of the plasmonic bowtie antenna. *Opt. Exp.* 2011;19:10456–10461.
- [46] Blanchard R, Boriskina SV, Genevet P, et al. Multi-wavelength mid-infrared plasmonic antennas with single nanoscale focal point. *Opt. Exp.* 2011;19:22113–22124.
- [47] Berrier A, Ulbricht R, Bonn M, et al. Ultrafast active control of localized surface plasmon resonances in silicon bowtie antennas. *Opt. Exp.* 2010;18:23226–23235.
- [48] Lin T-R, Chang S-W, Chuang SL, et al. Coating effect on optical resonance of plasmonic nanobowtie antenna. *Appl. Phys. Lett.* 2010;97:063106-1–063106-3.
- [49] Cetin AE. FDTD analysis of optical forces on bowtie antennas for high-precision trapping of nanostructures. *Int. Nano Lett.* 2015;5:21–27.
- [50] Sundaramurthy A, Crozier KB, Kino GS, et al. Field enhancement and gap-dependent resonance in a system of two opposing tip-to-tip Au nanotriangles. *Phys. Rev. B.* 2005;72:165409-1–165409-6.
- [51] Rechberger W, Hohenau A, Leitner A, et al. Optical properties of two interacting gold nanoparticles. *Opt. Commun.* 2003;220:137–141.
- [52] Fromm DP, Sundaramurthy A, Schuck PJ, et al. Gap-dependent optical coupling of single “bowtie” nanoantennas resonant in the visible. *Nano Lett.* 2004;4:957–961.
- [53] Novotny L. Effective wavelength scaling for optical antennas. *Phys. Rev. Lett.* 2007;98:266802-1–266802-4.
- [54] Guo H, Meyrath TP, Zentgraf T, et al. Optical resonances of bowtie slot antennas and their geometry and material dependence. *Opt. Exp.* 2008;16:7756–7756.